4. SPRAY PROCESSES

Submodels are discussed in this Section for the important processes that occur within sprays of practical interest. This includes models for the effects of drop breakup, distortion and drag, turbulent dispersion, drop collision/coalescence, and vaporization.

4.1 Drop Breakup

The effect of drop breakup on engine sprays was studied by Reitz and Diwakar (1986) who modeled experiments on hollow-cone sprays from an oscillating-poppet injector. In the experiments, indolene was injected into quiescent room temperature nitrogen at 307, 550, 1500 and 4712 kPa. The nozzle full-cone angle was θ=60, the seat diameter was δ=2.4 mm (see Fig. 3.9a). The flow rate was 0.0165 mL/injection with four pulses, each with a duration of about 0.58 ms, as determined from the measured liquid injection pressure shown in Fig. 4.1. The injection velocity was obtained from experimental spray tip velocity measurements early in each injection. The size of the injected drops (also shown in Fig. 4.1) was obtained from the sheet breakup correlation, Eq. 3.11, by assuming a sine-squared variation of poppet lift (or sheet thickness) with time, and the maximum poppet lift was found from the measured fuel flow and the injection velocity.

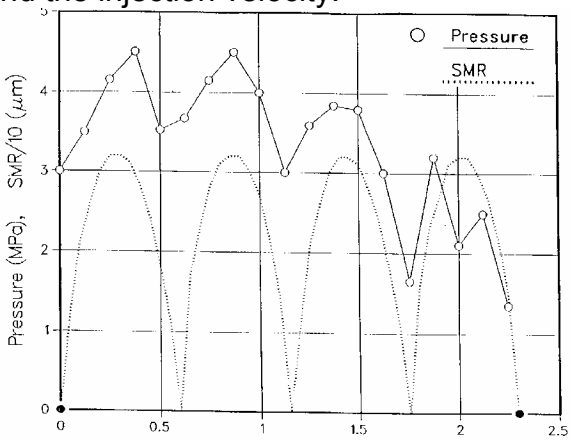

Fig. 4.1 Measured liquid injection pressure versus time (in ms) (Shearer and Groff, 1984). Dashed line shows the injected drop Sauter Mean Radius from Eq. (3.11) (Reitz and Diwakar, 1986).

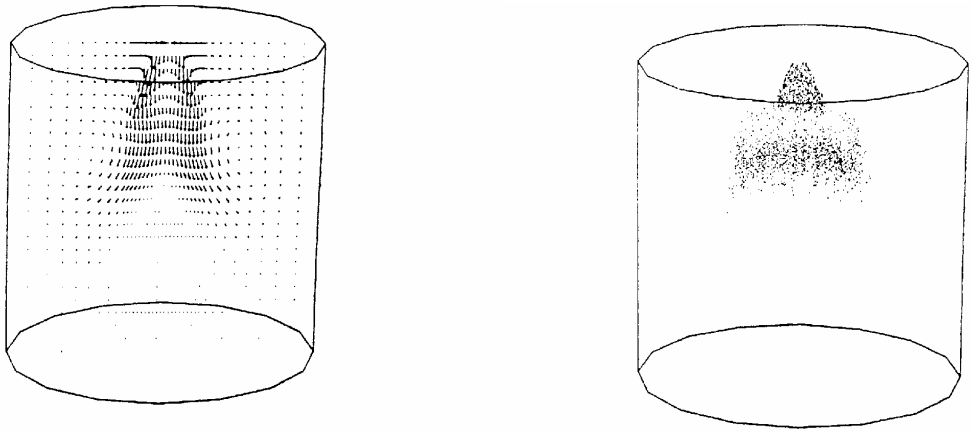

(a.) (b.)

Fig. 4.2 Predicted a.) gas velocity field b.) spray parcel locations at 2.1 ms after the beginning of injection (Reitz and Diwakar, 1986).

The computations were made using a cylindrical computational domain (diameter and height equal to 40mm - see Fig. 2.5) with the KIVA code (Amsden et al., 1985). As shown in Fig. 4.2, the injector was located at the top of the computational domain. Sample results showing the velocity field generated by the interaction of the drops with the gas, and the penetration of the drops into the chamber at 2.1 ms after the beginning of injection are given in Figs. 4.2a and 4.2b, respectively. As can be seen, a vortex is predicted to be present in the gas at the tip of the pulsed spray. The pulsed injection leads to clustering of the droplets and has the effect of increasing the radial extent of penetration and mixing. The region at the rear of the head vortex contains small entrained drops (Reitz and Diwakar, 1986).

Details of the temporal evolution of the spray seen in the experiments of Shearer and Groff (1984) are presented in the top frames of Fig. 4.3 which shows 12 consecutive movie frames at 0.222 ms between frames for the 550 kPa gas pressure case. Breaks in the spray occur at those points in time when the poppet closes, and the subsequent injections catch up and merge with the vortices produced at the tip of the spray during the previous pulses.

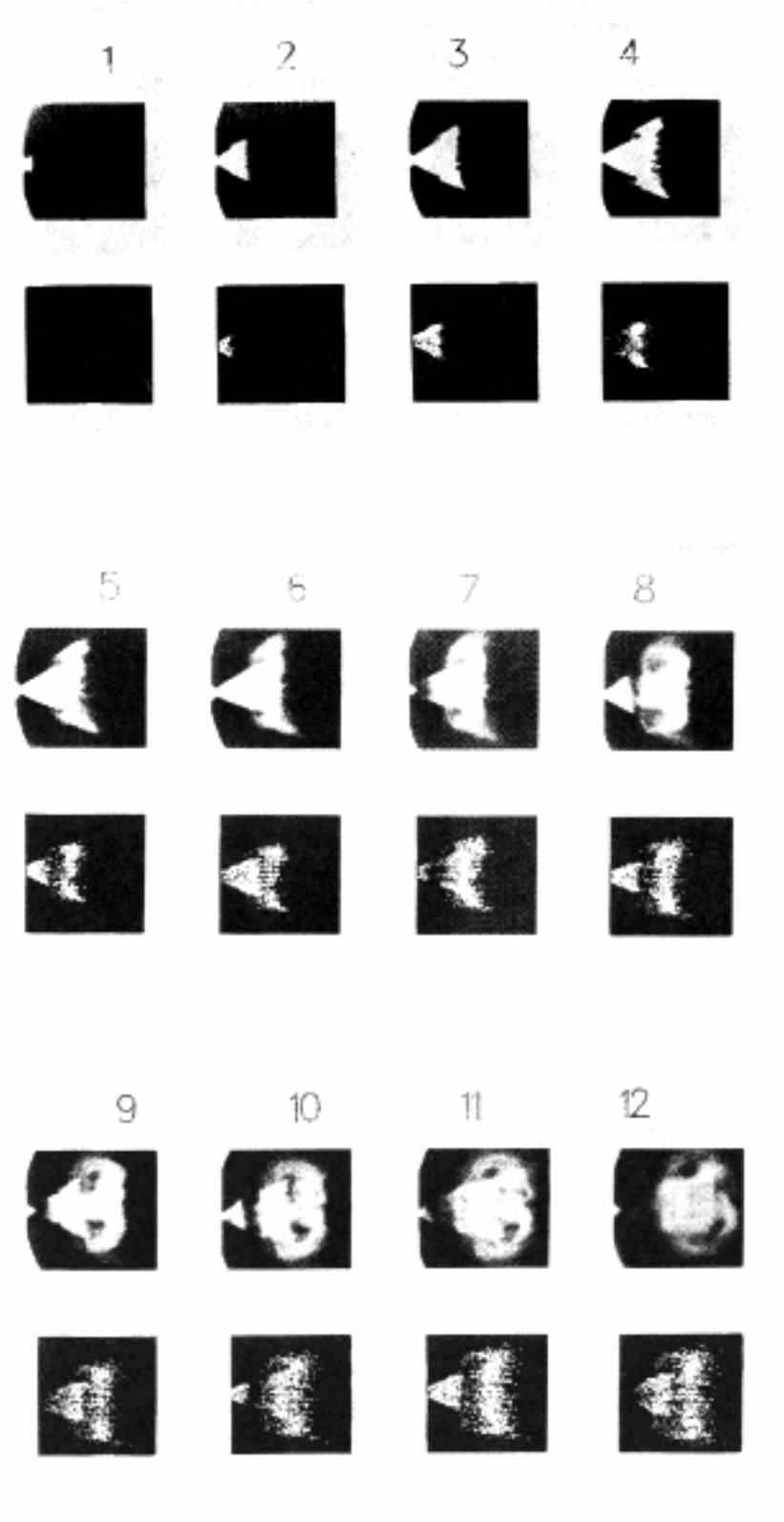

Fig. 4.3 Comparison of experimental (top frames) and computed (lower frames) sprays. 0.222 ms between frames.

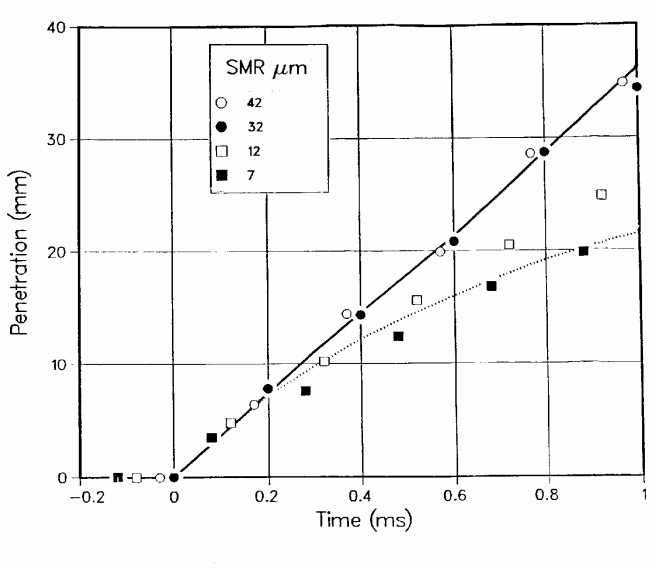

Fig. 4.4 Measured and computed spray tip penetration versus time.

Spray tip penetration measured from the movie frames is shown by the dotted line in Fig. 4.4. The figure also shows the predicted spray tip penetration without including drop breakup in the computations. The four different symbols correspond to the use of different values of the constant, D, in Eq. (3.11) (12, 20, 147 and 432 giving SMR=42, 32, 12 and 7 μm for the injected drop size at maximum poppet lift, respectively). It is seen that large D values (very small initial drop sizes) are required in order to match the experiment. The computed penetration was found to be insensitive to further reductions in the initial SMR beyond 7 μm. This is because the number of injected drops increases with decreasing initial drop size (for the same fuel flow) and drop collision and coalescences become more influential as the drop number increases, compensating for the smaller initial drop size. As seen in Fig. 4.4, the large 42 μm drops penetrate at constant velocity, in disagreement with the experimental result.

The very small initial drop size needed to match the experimental tip penetration is not consistent with other sheet breakup data which suggest that the initial SMR is between 30 and 40 μm (e.g., Dombrowski and Hooper, 1962, Lee and Bracco, 1994) for these low injection pressure sprays. This large discrepancy has prompted consideration of the effects of drop secondary breakup.

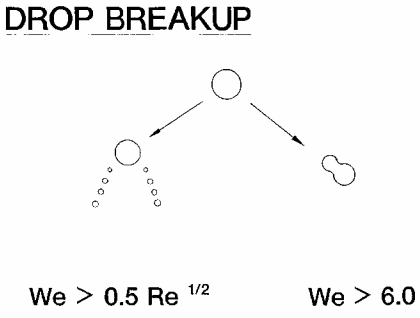

Fig. 4.5a Schematic diagram of drop breakup in the stripping (left) and bag (right) breakup regimes of Nicolls (1972).

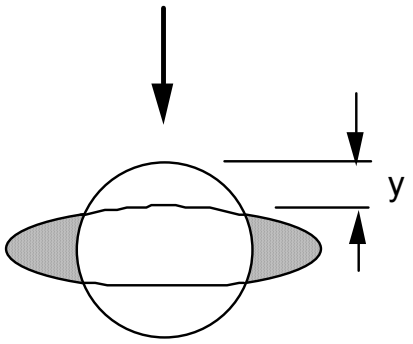

Fig. 4.5b Drop distortion computed using TAB model (O'Rourke and Amsden, 1986).

Reitz and Diwakar (1986) modeled drop breakup using correlations given in the review by Nicholls (1972) who identified two breakup regimes (see Fig. 4.5a): bag breakup when

$$We_g = \rho_g U^2 r / \sigma > 6.0 \qquad (4.1)$$

where We is the Weber number based on the gas density, r is the drop radius and U is the relative velocity between the drop and the gas, and stripping breakup when

$$We_g / \sqrt{\mathrm{Re}_g} > 0.5 \qquad (4.2)$$

where the Reynolds number $Re_g=2Ur/\nu_g$, and ν_g is the kinematic viscosity of the gas. The lifetimes of unstable drops are

$$t_1 = D_1 \sqrt{\frac{\rho_l r^3}{\sigma}} \qquad (4.3)$$

and

$$t_2 = D_2 \frac{r}{U} \sqrt{\frac{\rho_l}{\rho_g}} \qquad (4.4)$$

for the bag and stripping modes, respectively. The constants D_1 and D_2 are of order unity (Nicolls, 1972).

As a first attempt to account for drop breakup, Reitz and Diwakar (1986) adopted the following method and assumptions. The stability criteria, Eqs. (4.1) and (4.2), were checked for each drop parcel at each timestep. If either of the two criteria continued to be met for a time equal to the corresponding time in Eqs. (4.3) or (4.4), then a new drop size was specified for the parcel using either Eq. (4.1) or Eq. (4.2) (depending on which breakup criterion was exceeded) as an equality (i.e. it was assumed that the new drops were marginally stable).

Mass, momentum and energy conservation were assured during this 'breakup' procedure by adjusting the parcel drop number, n, with

$$n_f r_f^3 = n_i r_i^3 \tag{4.5}$$

where the subscripts f and i denote conditions after and before breakup, respectively. The drop surface energy also increases at breakup. The energy equation is

$$\tfrac{4}{3}\pi\rho_l r^3 n\,\mathbf{v}^2/2 + \pi\sigma r^2 n = \text{constant} \tag{4.6}$$

and to conserve energy, the drop's velocity components were each reduced by the factor δV, where

$$\delta V = 1 - \tfrac{3}{4}\left(\frac{r_i}{r_f} - 1\right)\frac{\sigma}{\mathbf{v}^2\rho_l r_i} \tag{4.7}$$

Equation (4.7) is a linearized form of Eq. (4.6). For consistency the momentum lost by the drops during this procedure, $m(\mathbf{v}_f - \mathbf{v}_i)$, was added to the gas momentum. As noted by Reitz and Diwakar (1986), these momentum and energy corrections were small for their sprays.

Koo and Martin (1991) made detailed measurements of drop sizes and velocities using Phase/Doppler anemometry. They concluded that a significant number of drops in high pressure sprays are unstable and subject to the bag and boundary-layer stripping mechanisms. These measurements thus provide some direct evidence of the importance of drop breakup in practical sprays.

The computed tip penetrations shown in Fig. 4.6 (symbols) include the effect of drop breakup. The corresponding experiments (lines) cover a broad range of gas pressures (factor of 15) (Shearer and Groff, 1984). The computations used D=20 in Eq. (3.11) and D_1=1.0 and D_2=0.5 in Eqs. (4.3) and (4.4). These values of the constants are consistent with published sheet and drop breakup data (e.g., Clark and Dombrowski, 1972, and Dombrowski and Hooper, 1962). It is seen that the calculations predict the experimental tip penetration adequately over the tested range of gas pressures.

Other calculations made with different values of D in Eq. (3.11) showed that the tip penetration and the downstream drop size are not very sensitive to the atomization drop size when drop breakup is included in the computation.

Details of the computed spray structure are presented in Fig. 4.3 for comparison with the photographs. The computed spray shape is seen to agree well with the experimental results throughout the four spray pulses. In particular, the vortex seen at the spray tip in the photographs is also evident in the computations. This confirms the importance of the effect of drop breakup in sprays since this vortex contains the small drops produced by the breakup process.

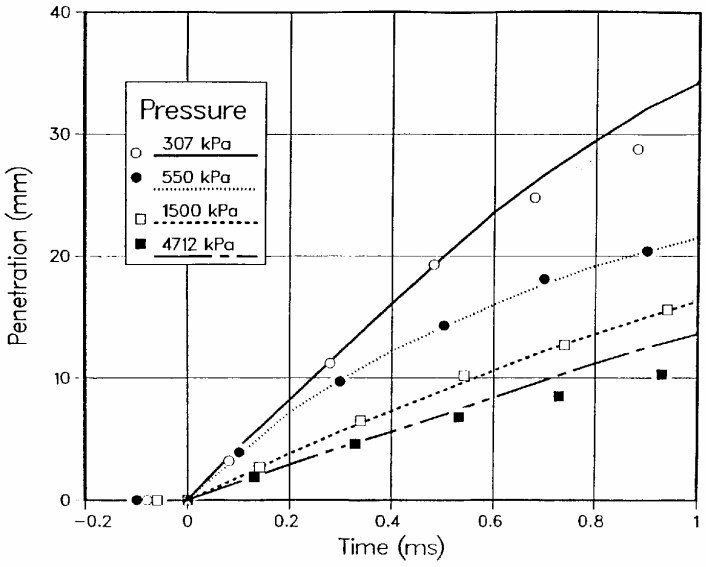

Fig. 4.6 Pulsed hollow-cone spray penetration versus time at various gas pressures. Lines - experiments (Shearer and Groff, 1984), symbols - computed (Reitz and Diwakar, 1986).

O'Rourke and Amsden (1986) proposed an alternative drop breakup model called the "TAB" (Taylor Analogy Breakup) model which is based on Taylor's (1963) analogy between an oscillating and distorting drop and a spring-mass system. The external force acting on the mass, the restoring force of the spring, and the damping force are analogous to the gas aerodynamic force, the liquid surface tension force, and the liquid viscosity force, respectively. The parameters and constants in the TAB model equations have been determined from theoretical and experimental results, and the model has been applied successfully to sprays by O'Rourke and Amsden (1986).

The distortion parameter, y=2x/r, (see Fig. 4.5b) (x is the displacement of the equator of the drop from its equilibrium position), is calculated by solving the spring-mass analogy equation,

$$\ddot{y} = \frac{2}{3}\frac{\rho_g U^2}{\rho_l r^2} - \frac{8\sigma}{\rho_l r^3} y - \frac{5\mu_l}{\rho_l r^2}\dot{y} \qquad (4.8)$$

where μ_l is the liquid viscosity and the dot indicates a time derivative. If it is assumed that the relative velocity between the drop and the gas, U is constant, then the solution to Eq. (4.8) is

$$y(t) = \frac{We}{12} + e^{-t/t_d}\{(y(0) - \frac{We}{12})\cos\omega t + (\frac{\dot{y}(0)}{\omega} + \frac{y(0) - \frac{We}{12}}{\omega t_d}\sin\omega t) \qquad (4.9)$$

where

$$t_d = \frac{2\rho_l r^2}{5\mu_l};$$

$$\omega = \frac{8\sigma}{\rho_l r^3} - \frac{1}{t_d^2}$$

O'Rourke and Amsden (1986) argued that when the value of y exceeds unity, the droplet breaks up into smaller droplets with the distribution of sizes specified as described below.

The breakup times that the TAB model predicts have been compared to experiments on drop breakup. For an inviscid liquid Eq. (4.9) shows that y>1 implies that

$$We = We_{crit} > 6.0 \tag{4.10}$$

which agrees with the experimental criterion for the onset of bag breakup in Eq. (4.1). When We is close to this critical value the breakup time is determined from Eq. (4.9) by assuming that $\omega t_{bu} = \pi$ (where t_{bu} is the breakup time), or

$$t_{bu} = \frac{\pi}{2}\sqrt{\frac{\rho_l r^3}{2\sigma}} \tag{4.11}$$

This agrees with the bag breakup time, t_1, in Eq. (4.3) if D_1=2. For We>>1, the drop breaks up after a short fraction of its oscillation period (i.e., ωt_{bu}<<1) and, when y=1 is assumed, Eq. (4.9) reduces to

$$t_{bu} = \sqrt{3}\frac{r}{U}\sqrt{\frac{\rho_l}{\rho_g}} \tag{4.12}$$

assuming an inviscid liquid. Equation (4.12) agrees with the "stripping" breakup time of Nicolls (1972) in Eq. (4.4) if D_2=1.73.

The TAB model has also been used to predict the velocity of the product drops normal to the path of the parent drop. At the time of breakup, Eq. (4.9) shows that the equator of the drop is moving outward at a velocity, $\mathrm{v} = r\dot{y}/2$ so, for inviscid liquids and We >>1,

$$\tan\frac{\theta}{2} = \frac{\mathrm{v}}{U} = C_v\frac{\sqrt{3}}{3}\sqrt{\frac{\rho_g}{\rho_g}} \tag{4.13}$$

where C_v is a constant. Equation (4.13) is very similar in form to the result given in Eq. (3.7) which agrees with experimental data (Reitz and Bracco, 1979).

O'Rourke and Amsden (1986) also presented a theory for the drop sizes after breakup of the parent drop. The theory assumes that the surface energy and the energy in the oscillation and distortion of the parent drop (the left-hand-side terms in Eq. (4.14), respectively)

$$4\pi r^2\sigma + K\frac{\pi}{5}\rho_l r^5(\dot{y}^2 + \omega^2 y^2) = 4\pi r^2\sigma\frac{r}{r_{32}} + \pi r^5\rho_l\dot{y}^2/6 \qquad (4.14)$$

is equal to the surface energy of the product drops plus their kinetic energy due to the acquisition of a velocity component normal to the path of the parent drop (right-hand-side terms of Eq. 4.14), where the constant K=10/3, and r_{32} is the Sauter Mean Radius of the product drops. This leads to the result

$$\frac{r}{r_{32}} = \frac{7}{3} + \frac{\rho_l r^3}{8\sigma}\dot{y}^2 \qquad (4.15)$$

Equation (4.15) reduces to $r_{32}=3r/7$ in the bag-breakup regime, while in the stripping breakup regime (We>>1) one gets

$$\frac{\rho_g U^2 r_{32}}{\sigma} = 6 \qquad (4.16)$$

which is the same expression used by Reitz and Diwakar (1986) who applied Eq. (4.1) as an equality to determine the product drop size. The use of Eq. (4.2) for determining the product drop size has been criticized by O'Rourke and Amsden who note that the equation includes the Reynolds number based on gas properties. Since the gas viscosity was not varied appreciably by the proposers of criterion (Nicolls, 1972), and the breakup times do not contain the gas viscosity, there appears to be little other justification for its use. In fact, Reitz (1987) has found that very similar equilibrium drop sizes result if the breakup criterion, Eq. (4.1) is always used to specify the product sizes, instead of Eq. (4.2).

Reitz (1987) has shown that the measured drop breakup correlations can also be recovered from the "wave" stability theory presented in Section 3. From the "wave" breakup theory, the breakup time is (see Eq. 3.15)

$$\tau = \frac{3.726\, B_1 a}{\Lambda \Omega} \tag{4.17}$$

where B_1 is the breakup time constant, and 'a' is the parent drop or jet radius. Substituting Eqs. (3.4a) and (3.4b) for the wavelength and wave growth rate of the most unstable surface waves, respectively, into Eq. (4.17), and considering an inviscid liquid in the low Weber number limit gives

$$\tau = 0.82 B_1 \sqrt{\frac{\rho a^3}{\sigma}} \tag{4.18a}$$

which is the same result as that derived in the TAB method, Eq. (4.11), if B_1=1.35. For inviscid liquids at large Weber numbers, Eq. (4.17) becomes

$$\tau = (B_1 a/U) \sqrt{\rho_1/\rho_2} \tag{4.18b}$$

which agrees with the TAB model result in Eq. (4.12) if $B_1 = \sqrt{3}$. As seen previously, the wave theory also gives an expression for the drop normal velocity component (Eq. 3.7) which agrees with Eq. (4.13) of the TAB model. There is considerable uncertainty about the value of the constant, B_1. For example, Reitz and Diwakar (1987) used B_1=20, Nicholls (1972) gave B_1=8.

Recent results indicate that the value of the breakup constant may need to be a function of initial disturbance levels to the drop in the flow (Kong and Reitz, 1995). Patterson et al. (1994) have used B_1=30 for diesel sprays (see Section 6.2, while Eckhause and Reitz (1994) and Liu et al. (1993) have found that $B_1 = \sqrt{3}$ is satisfactory for drops that are exposed to a violent disturbance.

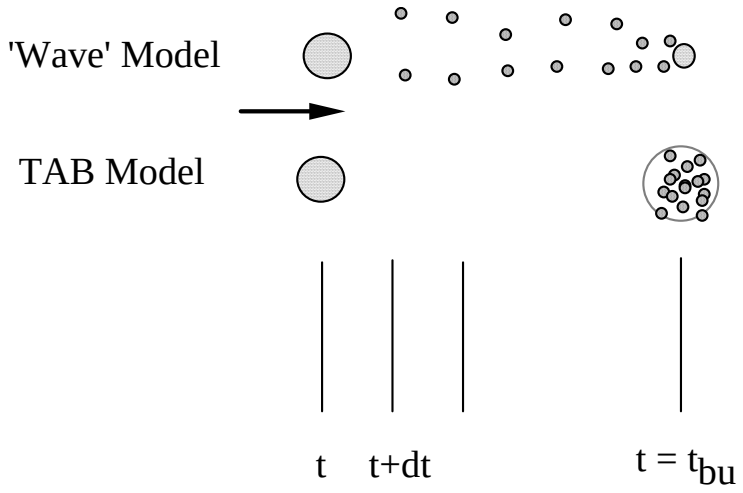

Fig. 4.7a Schematic diagram of drop breakup using the 'Wave' and TAB breakup models.

There are differences in the implementation of the 'wave' and TAB models that are summarized in Fig. 4.7a. In the TAB model, when the distortion parameter reaches unity, the drop is broken up, and, in the KIVA code (Amsden et al., 1989), the newly formed drops still belong to the same parcel that now contains smaller drops (indicated by the dotted circle in Fig. 4.7a). In the 'wave' model, drops are shed from the parent drop throughout the parent drop lifetime. New parcels of drops are added each timestep or, to prevent the number of parcels in the computation from becoming too large, when enough mass would have been shed from a parent to justify the addition of a new parcel to the computation. This difference has a significant effect on the fuel vapor distribution in a high-pressure spray because the small product drops vaporize very rapidly (Reitz, 1987), or in cases where the breakup time is much longer than the numerical (hydrodynamical) timestep. In the latter case, the flow around the parent drop may have changed significantly during the breakup time interval.

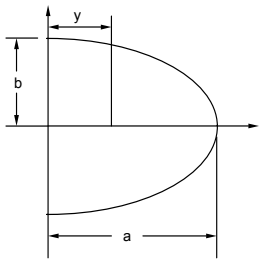

Fig. 4.7b The deforming half-drop of the DDB model (Ibrahim et al. (1993).

A modified version of the TAB model called the DDB (Dynamic Drop Breakup) model that enforces mass conservation constraints as the drop distorts has been used by Ibrahim et al. (1993) to predict drop breakup. The model is based on the dynamics of the motion of the center of mass of the half-drop. It is assumed that the liquid drop is deformed due to a pure extensional flow from an initial spherical shape of radius r into an oblate spheroid of an ellipsoidal cross section with major semiaxis a and minor semiaxis b. The internal energy of the half-drop comes from its kinetic and potential energies

$$\frac{dE}{dt} = \frac{2}{3}\pi r^3 \rho_l \frac{dy}{dt}\frac{d^2y}{dt^2} + \frac{9\pi^2\sigma}{8} y[1-2(\frac{cy}{r})^{-6}]\frac{dy}{dt}$$

where c=3π/4, y is the distance from the center of mass of the deforming half-drop to its equator, as shown in Fig. 4.7b. The work done is by pressure and viscous dissipation, which can be written as

$$\frac{dW}{dt} = -\frac{\pi}{4} r^2 \rho_g U^2 \frac{dy}{dt} + \frac{8}{3}\pi r^3 \mu_l (\frac{1}{y}\frac{dy}{dt})^2$$

Equating the internal energy and work rates with $y_1 = y/r$ and $t_1 = tU/r$ (r is the initial frop radius) gives for the drop distortion

$$\frac{d^2y_1}{dt_1^2} = \frac{3}{8K} - \frac{27\pi^2}{16KWe} y_1[1-2(cy_1)^{-6}] - \frac{4N}{K\,\mathrm{Re}}\frac{1}{y_1^2}\frac{dy_1}{dt_1} \qquad (4.19)$$

where $K=\rho_l/\rho_g$, $\mathrm{Re}=\rho_l U\, r/\mu_l$ and $N=\mu_l/\mu_g$. Model predictions made by Ibrahim et al. (1993) with the DDB model were found to agree well with experimental drop breakup results of Krzeczkowski (1980). Breakup was taken to occur when $a/r=We/6\pi$, where $We=\rho_g U^2 r/\sigma$.

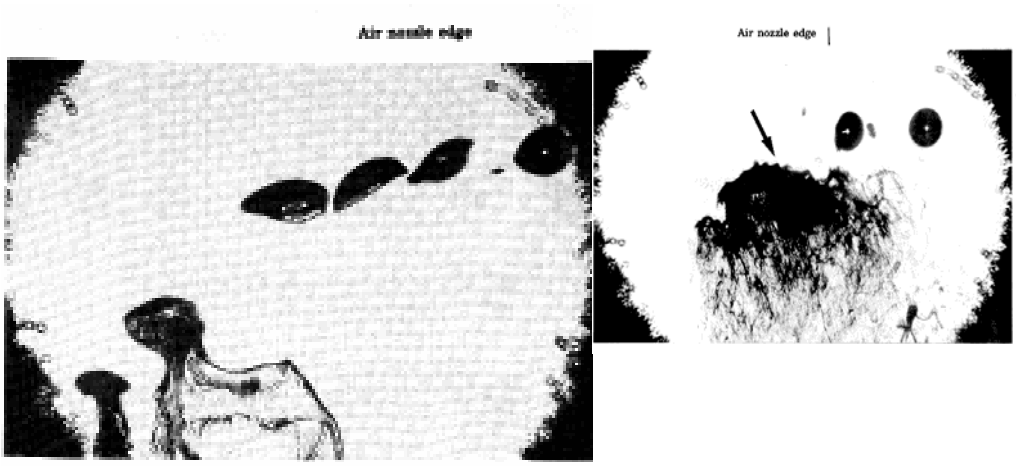

a.) b.)

Fig. 4.8 Photographs of 170 μm diameter diesel fuel drops being deflected and broken up by a 72 m/s (a.) and a 250 m/s (b.) transverse air jet. The drop stream enters the jet from right to left.

Most experimental studies on liquid drop breakup in the literature have considered the breakup of relatively low speed drops in the bag breakup regime (e.g., Kennedy and Roberts, 1990). As the relative velocity between a drop and the surrounding gas is increased, the drop distorts from its undisturbed spherical shape and ultimately the drop becomes flattened, or disk shaped, normal to the flow direction. At sufficiently high Weber numbers, the center of the disk deforms into a thin balloon- or bag-like structure which is stretched and swept off in the downstream direction (see Fig. 4.8a). The drops are flattened and form bag membranes as they are accelerated by the air flow. The rupture of the bag produces small droplets, while the liquid located in the rim of the distorted disk-shaped drop eventually breaks up into relatively large drops.

In the "stripping" breakup regime (e.g., Ranger and Nicolls, 1969) which occurs at very high relative velocities, droplet breakup is less well understood. The breakup process produces small drops which appear to be sheared off from the parent liquid drop. Figure 4.8b reveals that the unstable growth of short wavelength surface waves is involved in the breakup process, as indicated by the arrow.

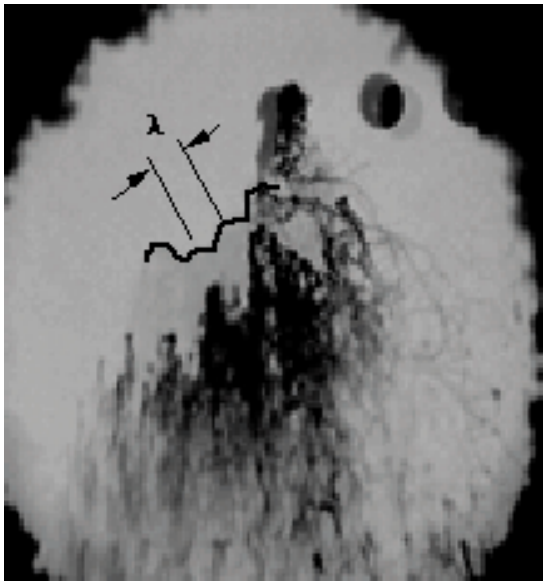

Fig. 4.8c Details of surface wave instability development in 'catastrophic' breakup regime from Hwang and Reitz (1995).

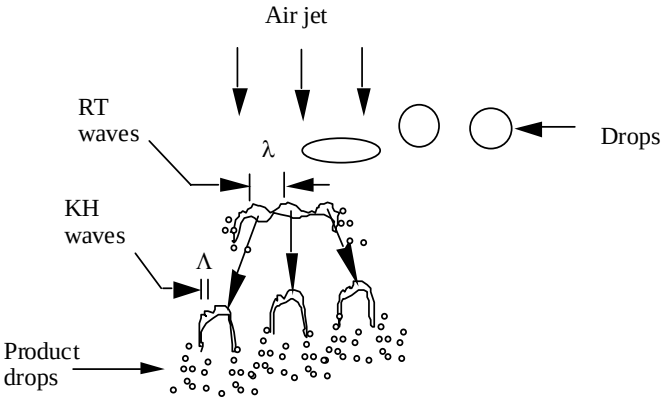

Fig. 4.8d Schematic diagram of drop breakup mechanisms in 'catastrophic' breakup regime.

The parent drop is distorted into a disk shape during the breakup process and it is surrounded by a shower of newly formed droplets which are rapidly swept downstream by the high velocity air jet. This type of breakup has also been referred to as 'catastrophic' breakup (e.g., Reinecke and Waldman, 1970).

The high-velocity drop breakup mechanism has been studied further by Hwang and Reitz (1995). Acceleration of the flattened drop favors the development of Rayleigh-Taylor (RT) instabilities seen in Fig. 4.8c, which shows two superimposed images of a drop taken 5 μs apart. Measured instability wavelengths, λ, were found to agree well with predictions from RT wave theory (Taylor (1950)), viz.

$$\lambda = 2\pi\sqrt{3\sigma / a(\rho_l - \rho_g)}$$

The accelerating drop breaks into large-scale fragments by means of RT instability. Much shorter wavelength Kelvin-Helmholtz (KH) waves originate on the fragmented surface and lead to ligament and small droplet formation, as illustrated schematically in Fig. 4.8d.

High speed droplet formation mechanisms are thus similar to the high velocity jet breakup mechanism in the second wind-induced and possibly also the atomization regimes, which involve the unstable growth of short wavelength surface waves.

Criteria for drop breakup regime transitions have been presented by Krzeczkowski (1980) and Wu et al. (1993). Consistent with the 'wave', TAB and DDB breakup models, the experiments of Wu et al. (1993) show that significant drop distortion and oscillation starts when $We_g > 1$. Bag breakup commences at about $We_g=6$. Transition to shear type breakup occurs at higher Weber numbers ($We_g > 80$) and 'multimode' breakup (combined bag- and shear-type) occurs in the intermediate Weber number range. For high viscosity liquids the Ohnesorge number must be introduced and the breakup regime transitions are moved to higher Weber numbers.

The TAB and DDB models have also been used to account for the effect of drop distortion on drop drag coefficients by Liu et al. (1993), Kong and Reitz (1995), and Hwang et al. (1995). These studies used the 'wave' model to describe the stripping of "children" drops from the distorted "parent" drop, as will be discussed next.

4.2 Drop Drag and Deformation

An important part of spray modeling is drop drag. Drop drag effects the drop's acceleration, and hence its velocity and physical location as a function of time. Basset (1888) presented the solution for the one-dimensional acceleration of a rigid particle under creeping flow (i.e., negligible convective acceleration) as

$$\mathbf{F} = 6\pi r \mu_g \mathbf{v} + \tfrac{1}{2}(\tfrac{4}{3}\pi r^3 \rho_g)\frac{d\mathbf{v}}{dt} + 6r^2\sqrt{\pi\mu\rho_g}\int_0^t \frac{d\mathbf{v}/dt'}{\sqrt{t-t'}}dt'$$

where μ_g is the gas viscosity, ρ_g is the gas density and $\mathbf{v}$ and r are the velocity and radius of the particle. The first term is the steady-state Stokes viscous drag, the second is the added-mass term resulting from the acceleration of the gas along with the particle, and the third is the Basset history integral. Additional terms that account for gas phase pressure gradients (on the scale of the drop) and Magnus lift effects have been neglected. The generalization of Basset's equation to three-dimensional flow is discussed by Clift et al. (1974), and the magnitude of the terms has been discussed by several researchers (e.g., Linteris et al., 1991). For typical spraying applications where the gas density is very much less than the liquid density, the added mass and Basset integral terms can be neglected.

The drop's acceleration is obtained from its equation of motion

$$\rho_1 V_d \, d\mathbf{v} / dt = \mathbf{F} = C_D A_f \rho_g U^2 \, / \, 2 \, \{\mathbf{U} / |\mathbf{U}|\} \qquad (4.20)$$

where U is the drop-gas relative velocity, $\mathbf{u}+\mathbf{u}'-\mathbf{v}$, and $V_d=4\pi r^3/3$, $A_f=\pi r^2$ are the volume, and frontal area, respectively (for a spherical drop), and ρ_1 and ρ_g are the liquid and gas density. If the gas velocity and the drop radius are assumed to be constant, Eq. (4.20) becomes

$$\frac{d\mathbf{v}}{dt} = \frac{9\mu}{2\rho_l r^2}(\mathbf{u}-\mathbf{v}) = (\mathbf{u}-\mathbf{v}) / \tau_m \qquad (4.21a)$$

where $\tau_m = 2\rho_l r^2 / 9\mu$ is the momentum relaxation time. Assuming $\mathbf{u}$=0

(quiescent gas), integration of Eq. (4.21) gives for the drop velocity

$$\mathbf{v} = \mathbf{v}_0 \exp(-t / \tau_m) \qquad (4.21b)$$

where $\mathbf{v}_0$ is the drop's initial velocity.

It is of interest to apply Eq. 4.21b to the data presented previously in Fig. 4.4 for hollow-cone spray injections into a pressurized gas. For the case where the injected drop radius is r=7 μm, the momentum relaxation time, τ_m, is about 0.12 ms (see Table 4.1). The predicted axial spray tip penetration is

$$S = \int_o^t \mathbf{v}\, dt = \mathbf{v}_o \tau_m (1 - e^{-t/\tau_m})$$

Thus, the maximum penetration of an injected drop (at large times) is predicted to be $\mathbf{v}_o\tau_m$ = 4.32 mm ($\mathbf{v}_o$=36 m/s). Of course, this does not agree with the measured data in Fig. 4.4 which shows that the spray reaches about 22 mm by 1 ms after the start of the injection

The use of Eq. (4.21b) to predict the penetration of transient thick or thin *sprays* is not justifiable because momentum transferred to the gas by the drops influences the state of the gas. The wake produced by drops at the tip of the spray reduces the relative velocity between the subsequent drops and the gas, and these drops experience "drafting" forces. The reduced drag on the subsequent drops allows them to overtake the leading drops at the tip of the spray, and the process repeats. Spray penetration is thus very much greater than would be predicted for single isolated drops with the same initial conditions.

Table 4.1 Droplet momentum relaxation times

	τ_m (ms)		
r (μm)	P_{gas}= 1	5	20 atm
1	0.01	0.002	0.0006
7	0.59	0.12	0.03
15	2.71	0.55	0.138

An additional consideration is that Stokes drag (which was assumed in deriving Eqs. (4.21)) only applies to flows at low drop Reynolds numbers (Re_d=U2r/ν_g, where 'r' is the drop radius). In most spray modeling applications, the drop Reynolds numbers are high enough that corrections to the Stokes drag law are required. For thin spray the drag coefficient, C_D, is often specified as a function of the drop Reynolds number using solid-sphere correlations, e.g., :

$$C_D = \frac{24}{Re_d}\left(1 + \frac{1}{6} Re_d^{2/3}\right) \qquad Re_d \le 1000 \tag{4.22a}$$

$$C_D = 0.424 \qquad Re_d > 1000 \tag{4.22b}$$

For thick sprays O'Rourke and Bracco (1980) replace Eq. (4.22a) with

$$C_D = \frac{24}{\mathrm{Re}_d}(\theta^{-2.65} + \mathrm{Re}_d^{2/3}\,\theta^{-1.78}/6) \tag{4.22c}$$

where θ is the local void fraction. Equation (4.22c) comes from experiments on fluidized beds and other sources (O'Rourke, 1981).

The effects of drop oscillation and distortion on the drop drag coefficient have been considered by Liu et al. (1993) and Hwang et al. (1995). At high relative velocities, the liquid drop deforms as it breaks up, and C_D is a function also of the oscillation amplitude. Liu et al. (1993) used the TAB model (see Section 4.1) to estimate the distortion of the drops, and the wave growth process that leads to the stripping of drops from the distorting liquid surface was modeled using the 'wave' or 'blob' breakup model. The drop drag coefficient was assumed to be related to the magnitude of the drop deformation with

$$C_D = C_{D,sphere}(1 + 2.632\,y) \tag{4.23}$$

where the amplitude of the drop's surface oscillation was calculated dynamically as a function of the flow conditions using the TAB model Eq. (4.8). Equation (4.23) expresses the fact that the drag coefficient of a distorting drop should lie between that of a rigid sphere and that of a disk, whose drag coefficient at high Reynolds numbers is about 3.6 times higher than that of a sphere.

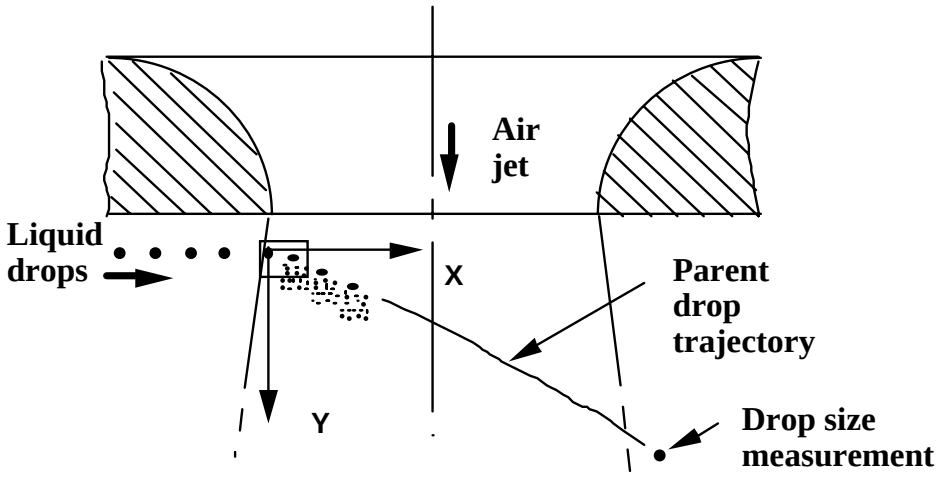

Fig. 4.9 Schematic diagram of drop breakup experiment of Liu and Reitz (1993). 170 μm diameter monodisperse liquid drop stream enters transverse air-jet at 16 m/s. Square shows region photographed in the high magnification pictures of Fig. 4.8. Air nozzle diameter 9.5 mm.

The spray model was evaluated using measured trajectories and drop sizes of single drops injected into a high relative velocity gas flow using the configuration shown in Fig. 4.9. The apparatus consisted of a Bergland-Liu drop generator and an air nozzle with a converging exit, arranged in a cross flow pattern. The drop sizes were measured with a Phase Doppler Particle Analyzer (PDPA), and high magnification photographs were taken of the breakup process (see Figs. 4.8). This experimental configuration is useful because the relatively low liquid and spray drop density does not favor collisions and coalescences of the drops which complicate the interpretation of typical diesel spray experiments (see Section 4.4).

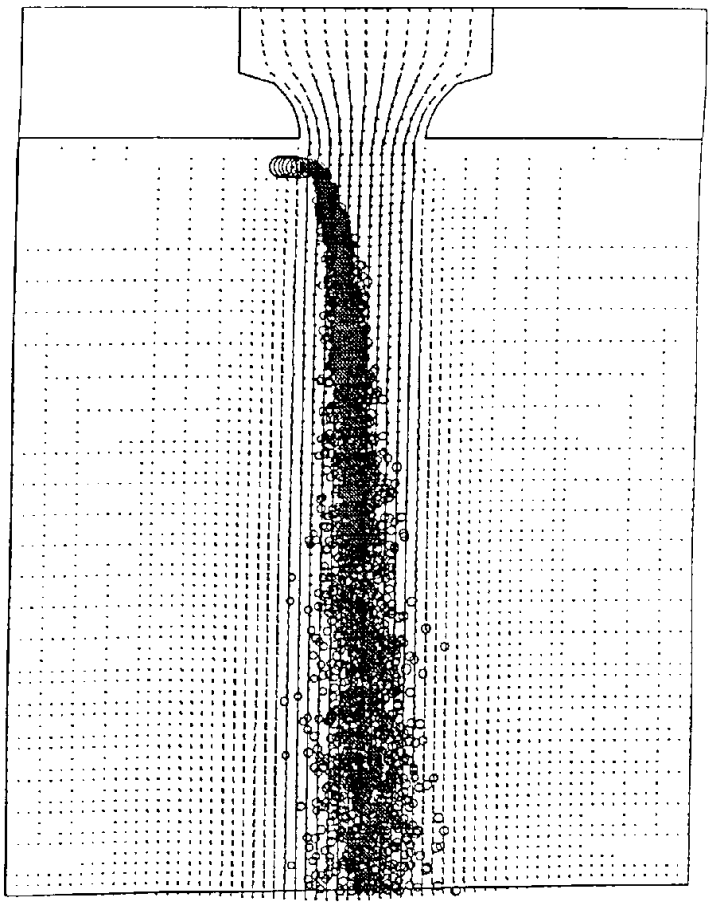

Fig. 4.10 Computed drop locations and gas velocity vectors for air jet velocity of 100 m/s (Liu et al., 1993). Monodisperse drop stream is injected into the airjet just below the nozzle exit plane from left to right.

The computations were made using a modified version of the KIVA-II code (Amsden et al., 1989). The 3-D computational mesh had 32x16x84 cells in the radial, azimuthal and axial directions, respectively. Figure 4.10 shows computed drop locations and gas velocity vectors in the plane of the nozzle, 4 ms after the start of the injection for a case with an air velocity of 100 m/s at the air nozzle exit. As can be seen, the horizontally injected drops are predicted to breakup into a spray of fine drops which are deflected by the air-jet.

Details of the deformation of a drop as a function of the horizontal distance, X, that it penetrates into the air-jet are given in Fig. 4.11. The liquid drop Reynolds number and the distortion parameter, y, are shown in Figs. 4.11a and b. The drop size and the instantaneous drag coefficient are plotted in Fig. 4.111c and d. These results apply to an individual drop interacting with the flow.

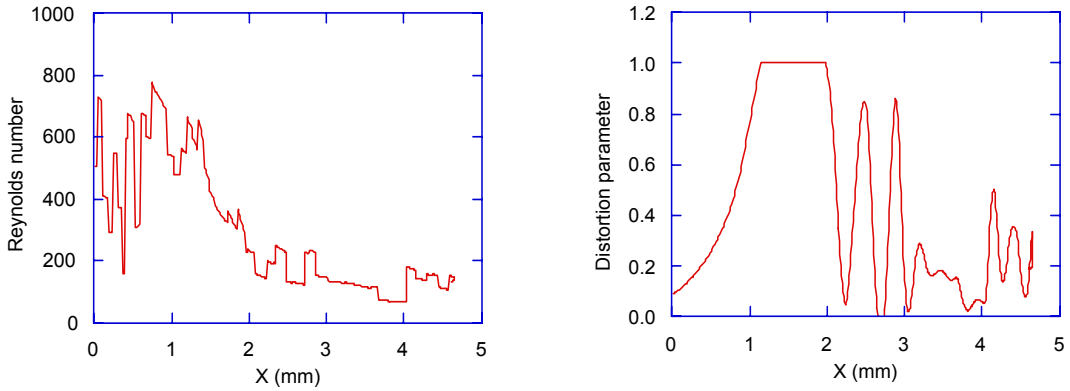

(a.) (b.)

Fig. 4.11 a.) Drop Reynolds number and b.) distortion parameter as a function of horizontal penetration distance, X, into the air jet. Air jet velocity of 100 m/s, dynamic drag model and 'wave' breakup model with B_1=1.73.

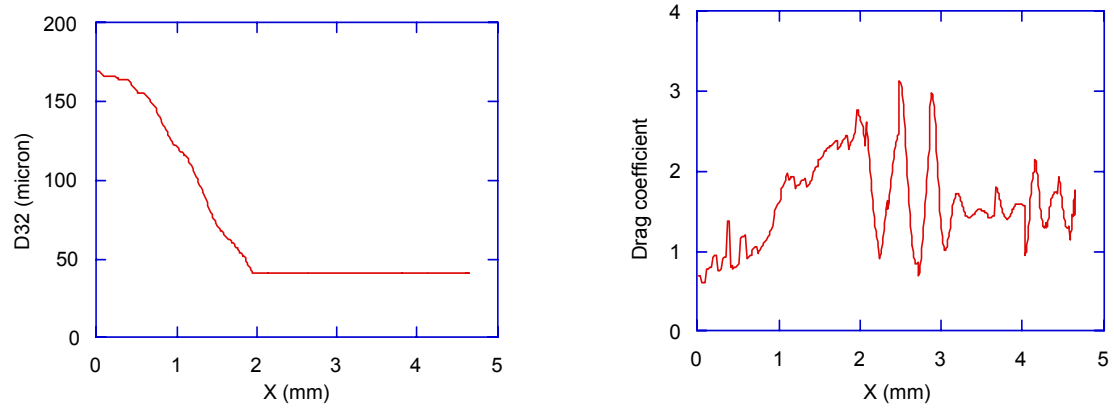

(c.) (d.)

Figure 4.11 c.) Drop diameter and d.) drag coefficient as a function of horizontal penetration distance, X, into the air jet. Air jet velocity of 100 m/s, dynamic drag model and 'wave' breakup model with B_1=1.73.

The (parent) drop diameter is seen in Fig. 4.11c to decrease continuously as the drop penetrates into the air jet due to (stripping) breakup of the liquid, and breakup ceases beyond about X=2 mm. The Reynolds number increases rapidly to a peak value due to the increase in the relative velocity between the drop and the gas as the drop enters the air jet. The Reynolds number then decreases, following the trend of the drop size variation, with fluctuations due to the gas turbulence.

The drop distortion parameter soon increases to the fully deformed drop maximum value of y=1, and remains at this value until the drop size is reduced sufficiently by the breakup process, and (or) the drop-gas relative velocity is reduced by the acceleration of the drop. The distortion parameter then decreases. The decrease is accompanied by large fluctuations indicating that the final parent drop is only marginally stable. Even after drop breakup ceases, oscillations are still visible in the drop drag coefficient due to the drop surface oscillations. These fluctuations are caused by the interaction of the liquid drops with the turbulent eddies of the air jet.

Measured and predicted (parent) drop trajectories are compared in Fig. 4.12a, which shows that good agreement with the

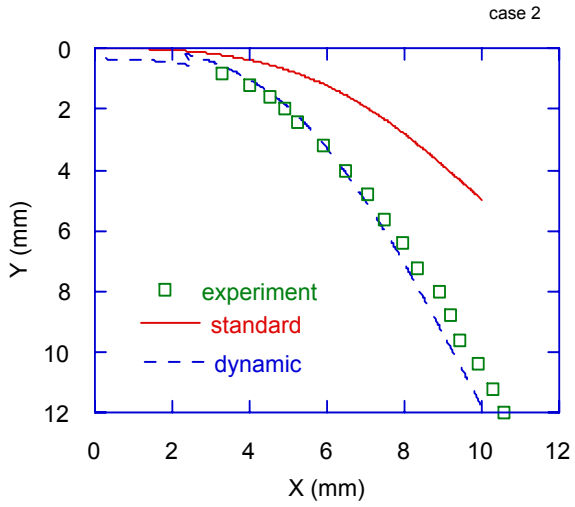

Fig. 4.12a Comparison of 'wave' breakup model predictions and measured drop trajectory for air jet velocity 59 m/s. Solid line - standard drop drag, dashed line - dynamic drag model.

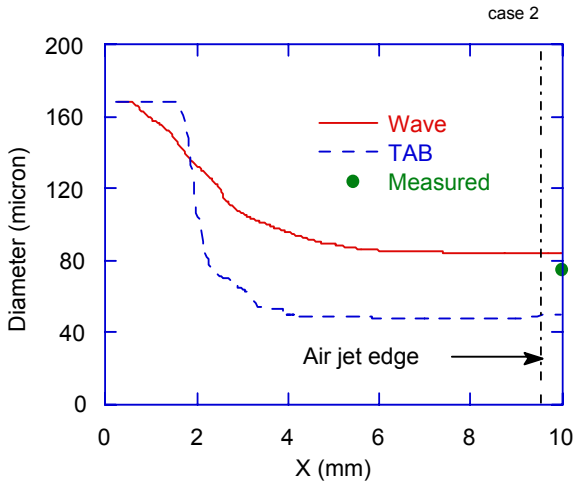

Fig. 4.12b Predicted drop Sauter mean diameter variation with distance across the jet for air jet velocity 59 m/s using the wave (solid line) and TAB (dashed line) models. Solid circle shows PDPA measured drop diameter outside air jet.

measured trajectories can be obtained with the modified drag coefficient that accounts for the fact that the parent drops are deformed by the gas flow as they breakup.

The predicted drop size variation across the air jet is shown in Fig. 4.12b using the 'wave' and TAB breakup models . In the 'wave' model, the (parent) drop size is predicted to decrease continuously within the jet, and the final (stable) drop size reached by drops that penetrate all the way through and emerge from the other side of the air jet is seen to be in good agreement with the measured drop size at the jet edge. In the TAB model, the breakup is more abrupt, as was discussed in Fig. 4.7, and the final drop size prediction is seen to under estimate the measured drop size significantly.

The trajectory of a drop is effected by both its breakup rate and the drag forces acting on it. In the model of Liu et al. (1993), these two effects are represented by the "wave" model breakup time model constant, B_1, and the drop drag coefficient, C_D, respectively. To validate spray models and their parameters, both the trajectory and size data must be compared with experimental data simultaneously, as was done in Figs. 4.11 and 4.12 above. Validation of drop breakup models is much more difficult in practical sprays because of a lack of accurate size and position measurements.

Liu et al. (1993) determined that the optimal value of the breakup constant was B_1=1.73, which agrees that suggested by O'Rourke and Amsden (1986). To account for secondary atomization for sprays that impinge on a wall, Kong and Reitz (1995) and Eckhause and Reitz (1994) have used B_1=1.73 (see Section 5.3). However, other computations have indicated that the value of the model constant depends on the flow situation. For example, for modeling diesel sprays, Patterson et al. (1993) have used B_1=30.

Interestingly, the results of Liu et al. (1993) show that spray tip penetration is relatively insensitive to the value of the drop drag coefficient for non-vaporizing diesel-type sprays. This is because changes in drop drag produce changes in the drop-gas relative velocity. This, in turn, causes changes in the spray drop size through the drop breakup and coalescence processes. The changes occur in such a way that the net effect on the spray penetration is small over the tested ranges of conditions. However, the dynamically varying drag coefficient has been found to be very important in modeling vaporizing sprays (e.g., Kong and Reitz, 1995) (see Section 6.2).

The high resolution photographs of Hwang et al. (1995) have been used to help study drop trajectories for highly accelerating drops. As noted in Figs. 4.8, the drops undergo significant flattening due to the dynamic pressure effect as soon as they enter the air jet. The flattening occurs prior to significant mass loss from the drops due to breakup. Both the TAB and DDB models were used for comparisons with the experiments. For the DDB model the drop frontal area in Eq. (4.20) was modified to account for the distortion using $A_f=\pi a^2$ for $a<2.7r$ (the DDB model predicts drop breakup when the ellipse major semi-axis, $a=3\pi/4y$, (see Eq. (4.19) and Fig. 4.7b) exceeds 2.7 times the initial undisturbed drop radius, r). In addition, the drag coefficient in Eq. (4.23) was calculated with $y = \min(1, \{\frac{a}{r} - 1\})$, so that the drag coefficients of a spherical drop and a disk were recovered in the undistorted and distorted drop limits, respectively.

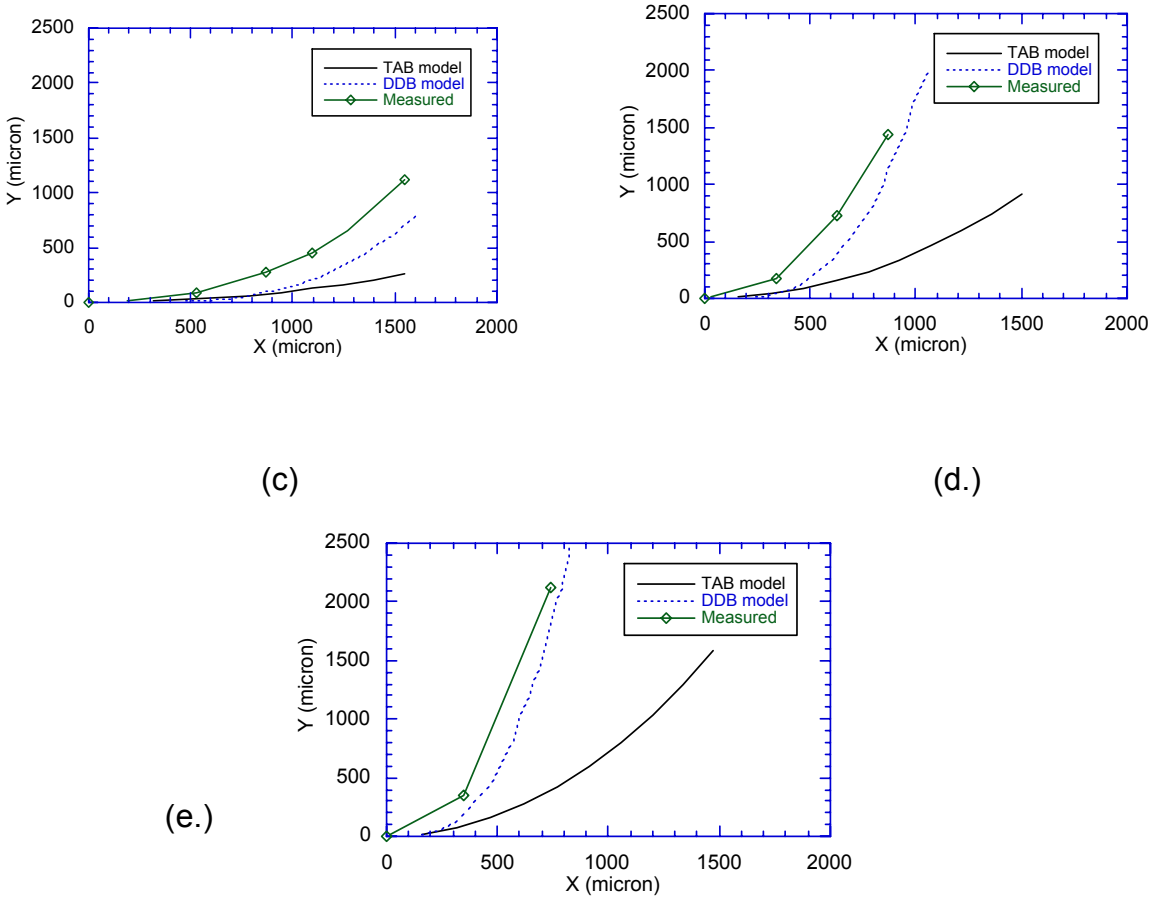

Fig. 4.12 (cont.) Measured and computed drop trajectories using the TAB and DDB models with different gas jet velocities, U.
c.) U=77, d.) U=150, e.) U=200 m/s (Hwang et al. (1995).

Figures 4.12c, d and e show the drop trajectories predicted using the TAB and DDB models for different gas velocities together with the experimental data. The solid curves are the results predicted by using the TAB model. The dotted curves represent the drop trajectories predicted by using the DDB model. There are large differences between the results predicted using the two models that are mainly due to the neglect of the increased frontal area of the flattened drop in the TAB model. The results calculated by using the DDB model are in good agreement with the measured data. These results indicate that the increased frontal area of the drop needs to be considered in drop breakup and spray computations as well.

4.3 Turbulence Diffusion and Modulation

The dispersion (or diffusion) of particles by turbulence is important in many industrial and energy-related processes and is reviewed for example by Crowe et al. (1988) and Lazaro and Lasheras (1989). The gas phase turbulence is modulated (reduced) since a portion of the turbulence energy is used to do work in dispersing the spray drops, as reviewed by Faeth (1983). However, as pointed out by Crowe (1993), the turbulence energy can also be increased if the drops are larger than about 1/10 of the integral scale of turbulence since their wakes represent a source of turbulence energy. This effect has not been modeled satisfactorily, even with DNS models.

Currently the most popular approach to predicting particle dispersion in turbulence is a Monte-Carlo method where the turbulent field is represented by a random number generator. The gas velocity is considered as the sum of the time-averaged (mean) velocity (denoted here with the overscore) and a fluctuating (turbulent) velocity (denoted with a prime)

$$\mathbf{u} = \overline{\mathbf{u}} + \mathbf{u}' \tag{4.24}$$

where $\mathbf{u}'$ is obtained from the turbulence model. Gosman and Ioannides (1981) combined this concept with the turbulence energy and dissipation rate (k-ε) equations. The turbulent fluctuation velocity is selected from a Gaussian distribution with a variance proportional to the turbulence kinetic energy, $|\mathbf{u}'|^2 = 2k/3$, i.e.,

$$G(\mathbf{u}') = \left(4/3\pi k\right)^{-3/2} \exp(-3|\mathbf{u}'|^2/4k)$$

The drop motion is integrated with this velocity field until it passes from the eddy. The drop-eddy interaction time is determined by the eddy life time, or by the time taken by the drop to pass through an eddy. The dissipation length and time scales are given by (see Fig. 2.9)

$$l = C_\mu^{3/4} k^{3/2} / \varepsilon \tag{4.25a}$$

$$t_e = l / \sqrt{2k/3} \tag{4.25b}$$

where k is the turbulence energy, ε is the dissipation rate and the constant C_μ=0.09 (see Eqs. (2.17) and (2.18)). The time taken to pass through an eddy is approximated as

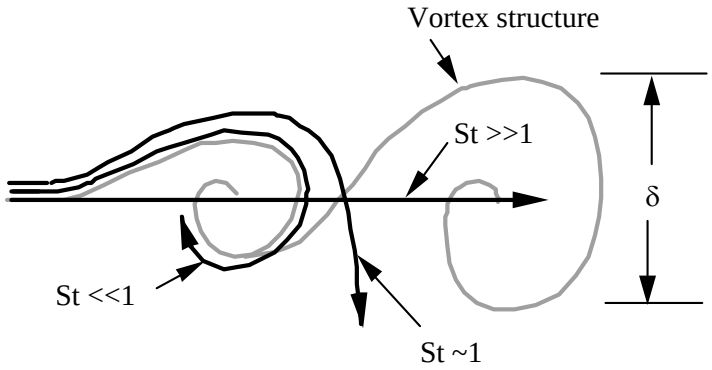

Fig. 4.13 Effect of Stokes number on particle dispersion in large-scale turbulent structures (Crowe et al., 1988).

$$t_p = 1 / |\bar{\mathbf{u}} - \mathbf{v}|$$

where $\bar{\mathbf{u}}$ is the mean gas velocity and $\mathbf{v}$ is the particle velocity. The interaction time, t_{int}, is the minimum of the eddy lifetime, t_e, and the passage time, t_p, i.e.,

$$t_{\text{int}} = \min(t_e, t_p) \qquad (4.26)$$

Crowe et al. (1988) have observed that small drops in a turbulent flow tend to follow the gas flow, and give a good visualization of the large eddies. However, the larger drops with their smaller drag/inertia ratios, leave the large-scale vortex structures. A time-scaling ratio was proposed which, assuming Stokes drag for the particles, gives the Stokes number

$$St = \tau_m / \tau_F = 2\rho_l r^2 \Delta U / 9\mu\delta \qquad (4.27)$$

where $\tau_m = 2\rho_l r^2/9\mu$ is the aerodynamic response time (see Eq. (4.21a). $\tau_F = \delta/\Delta U$ is the timescale associated with large scale structures with characteristic size δ, and ΔU is the velocity difference across the structure. As depicted in Fig. 4.13, particles with small Stokes numbers maintain near velocity equilibrium with the fluid and disperse as a fluid particle. Particles with St~1 can be "centrifuged" by the eddy and the particle dispersion can exceed that of a fluid particle. For large Stokes numbers, the large-scale structures have insufficient time to influence the particle motion.

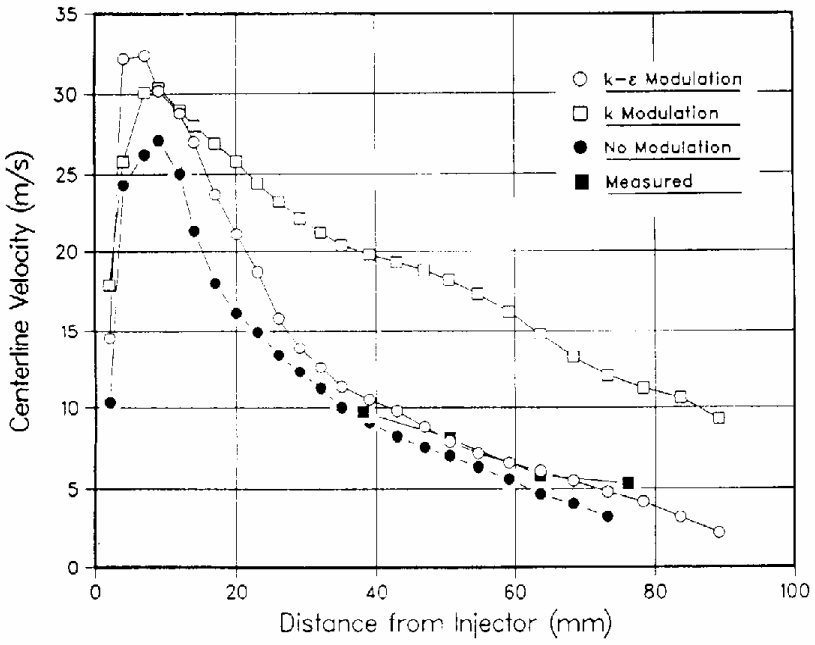

Fig. 4.14 Effect of turbulence modulation on gas centerline velocity decay (Reitz and Diwakar, 1987).

The interaction of the spray drops with turbulence reduces the rate of production of turbulence kinetic energy. A portion of the turbulence energy is used to do work in dispersing the spray drops. Since u' follows a Gaussian distribution it can be shown that $\dot{W}^s$<0 in Eq. (2.26), thus the drops always deplete the turbulence kinetic energy (Amsden et al., 1989). For incompressible turbulence in the absence of gradients, Eqs. (2.17) and (2.18) become

$$\rho\frac{dk}{dt} = \dot{W}^s, \qquad \rho\frac{d\varepsilon}{dt} = C_s\frac{\varepsilon}{k}\dot{W}^s \quad \text{or} \quad \frac{\partial}{\partial t}\ln k^{C_s}/\varepsilon = 0$$

Thus, the choice of the model constant C_s=3/2 in Eq. (2.18) assures that the turbulence length scale is unchanged by turbulence modulation (see Eq. (4.25a)). The implications of this assumption are discussed by Reitz and Diwakar (1987) who note that the effect of turbulence modulation is most important in the jet development region close to the nozzle in high pressure sprays. Figure 4.14 shows their jet centerline velocity decay predictions for a non-vaporizing high-pressure diesel spray, injected at 127 m/s through a 0.127 mm diameter (l/d=4) nozzle into a 4.24 MPa nitrogen environment. The

computed results with and without turbulence modulation agree well with measured velocities obtained by Wu et al. (1984) (shown by solid squares 40 to 80 mm from the nozzle).

The velocity decay is the fastest when turbulence modulation is not included (solid circles). The shape of the curves in the final decay region is similar, indicating that the main effect of the modulation is a shift in the virtual origin of the spray. The open squares show results with modulation only included in the k equation. Without the corresponding term in the ε equation, the reduced values of k lead to lower turbulence diffusivities in the developing jet (see Eq. 2.16). This produces an over-estimate of the spray penetration, which is governed primarily by the gas-phase turbulence diffusivity (Reitz and Diwakar, 1987).

4.4 Drop collision and Coalescence

Drop collision and coalescence phenomena become increasingly important in dense sprays. As depicted in Figs. 4.15, for binary collisions between drops the outcome may result in coalescence or separation, depending on the operating conditions, as described by Jiang et al. (1992) and Ashgriz and Poo (1990).

The collision regimes are shown in Fig. 4.15a which presents a (non-dimensional) impact parameter, x, (proportional to the distance between centers of the colliding drops) versus the collision Weber number, $We = \rho_L d_s u^2/\sigma$ (d_s is the smaller drop's diameter and u is the relative velocity between the two drops). x = 0 represents a head-on collision, while x=1 is a tangential or grazing collision. The symbols show experimental results, while the lines show collision regime boundaries inferred from the experiments.

As can be seen, for a fixed value of the impact parameter (i.e., a fixed orientation for the colliding drops), coalescence occurs at low drop collision Weber numbers. Separation of the colliding drops occurs as the Weber number is increased beyond a critical value (in stretching or reflexive modes).

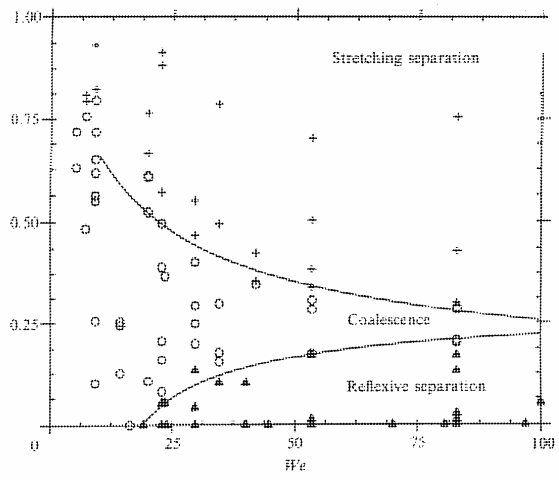

Fig. 4.15a Binary drop collision coalescence and stretching and reflexive separation regimes (Ashgriz and Poo, 1990)

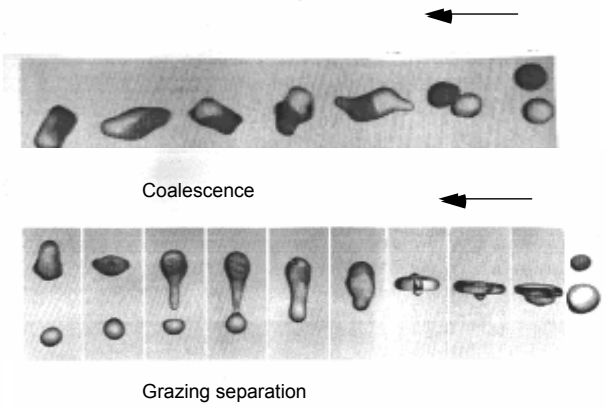

Fig. 4.15b Photographs of drop collision and coalescence and reflexive separation regimes (Ashgriz and Poo, 1990)

O'Rourke (1981) and O'Rourke and Bracco (1980) developed a method for computing drop collisions in sprays.

Following the reasoning used in the kinetic theory of gases, a collision frequency ν_{12} can be defined between drops in parcel 1 (containing the larger drops) and parcel 2, and is calculated in each computational cell using

$$\nu_{12} = N_2 \pi (r_1 + r_2)^2 E_{12} |\mathbf{v}_1 - \mathbf{v}_2| / Vol \qquad (4.28)$$

N_2 is the number of drops in parcel 2, $\mathbf{v}$ is the drop velocity vector and *Vol* is the volume of the cell. The drops may be deflected away from each other due to the changing gas velocity fields that the drops experience as they approach each other. This effect is accounted for by introducing the collision efficiency, E_{12}, which is the ratio of the actual collision cylinder swept out by the colliding drops in time Δt, to the ideal collision cylinder, $\pi(r_1 + r_2)^2 |\mathbf{v}_1 - \mathbf{v}_2| \Delta t$, which applies when the drops follow straight line trajectories.

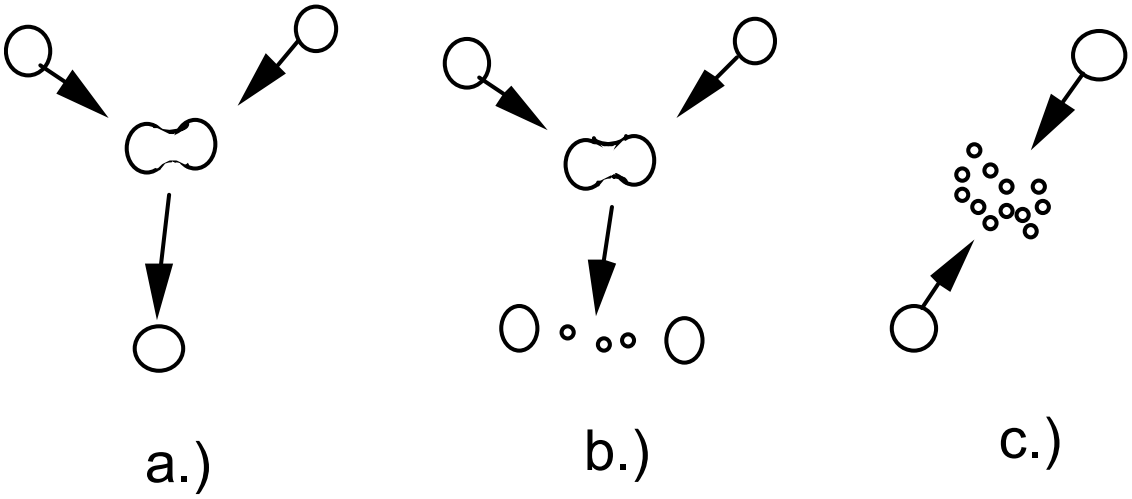

Fig. 4.15 Possible outcomes of a binary collision as the collision Weber number is increased. a.) permanent coalescence, b.) collision followed by breakup, c.) shattering (O'Rourke, 1981).

For small drops interacting with large "collector" drops, Langmuir (1948) found that the collision efficiency depends on the flow regime. For "aerodynamic" flow around the collector drop. i.e., for $\rho_g|\mathbf{u}-\mathbf{v}|r_1/\mu_g >> 1$

$$E_{12} = \left(\frac{K}{K+1/2}\right)^2 \qquad (4.29a)$$

For "viscous" flow, i.e., $\rho_g|\mathbf{u}-\mathbf{v}|r_1/\mu_g << 1$, Langmuir found

$$\begin{aligned} E_{12} &= \{1+\tfrac{3}{4}\ln[2K/(K-1.214)]\}^{-2} \quad \text{for} \quad K > 1.214 \\ E_{12} &= 0 \qquad\qquad\qquad\qquad\qquad\quad \text{for} \quad K \le 1.214 \end{aligned} \qquad (4.29b)$$

where

$$K = \frac{2}{9}\frac{\rho_l|\mathbf{v}_1-\mathbf{v}_2|r_2^2}{\mu_g r_1}$$

is approximately the ratio of the stopping distance of the smaller drop (with initial velocity $\mathbf{v}_1$-$\mathbf{v}_2$ relative to the gas) to the radius of the collector drop (see Eq. (4.21a). When K is small, E_{12} goes to zero because the drop is carried around the collector drop by the air flow. For large K, $E_{12} \sim 1$. Most computer modeling studies have assumed that E_{12}=1.0, consistent with order of magnitude estimates of O'Rourke (1981).

The probable number of collisions, *n*, was assumed by O'Rourke (1981) to follow the Poisson distribution

$$p(n) = e^{-\nu_{12}\Delta t}(\nu_{12}\Delta t)^n/n! \qquad (4.30)$$

where Δt is the computational time step and *p(n)* is chosen stochastically from the uniform distribution in the interval (0,1).

The outcome of a binary drop collision depends on forces acting on the coalesced pair of drops. As depicted in Fig. 4.15a, at low relative velocities, surface tension forces will dominate over liquid inertia forces, and the drops will coalesce permanently. The ratio of these two forces is the Weber number, $We_l = \rho_l|\mathbf{v}_1-\mathbf{v}_2|^2 r_1/\sigma$. At higher Weber numbers, the liquid inertia forces dominate, and the drops separate, possibly forming satellite droplets, as depicted in Fig. 4.15b. These are called "grazing" collisions by O'Rourke (1981). At very high relative velocities, the drops may shatter (Fig. 4.15c).

To determine the outcome of a collision, a collision impact parameter, b, is calculated and compared to a critical value, b_{crit}. If b is less than b_{crit}, the droplets coalescence. Physically, droplet separation occurs following a collision if the rotational energy of the coalesced pair exceeds the surface energy required to re-form the original drops from the coalesced pair. A coalescence efficiency, $E_{coal}=b/b_{crit}$, is defined by O'Rourke (1981) that depends on the drop radii before collision and the Weber number based on the drop velocity difference, where

$$b^2 = q(r_1 + r_2)^2$$

and

$$b_{crit}^2 = (r_1 + r_2)^2 Min(1.0, 2.4(\gamma^3 - 2.4\gamma^2 + 2.7)/We_1) \qquad (4.31)$$

where q is the random number in the interval of (0,1) and $\gamma=r_1/r_2$ is always greater than or equal to unity. As noted by MacInnes and Bracco (1991), from Eq. (4.31) it can be seen that drops of greatly unequal size will be more likely to coalesce than drops of nearly equal size. If the coalescence is predicted, n drops are removed from parcel 2 and the size, velocity, and temperature of drops in parcel 1 are modified appropriately to conserve mass, momentum and energy.

In a grazing collision, b exceeds b_{crit}, and the drops do not combine, but maintain their sizes and temperatures. The drops do undergo velocity changes that reflect momentum conservation considerations (O'Rourke, 1981, Amsden et al., 1989). The possible formation of satellite drops as a result of the collision has not been included in current models. Shattering collisions have also not been included. O'Rourke (1981) observes that experimental data indicates that shattering collisions have not been observed for $We_1 < 40$. This criterion is consistent with criteria for the onset of breakup of drops that impinge on walls, as will be discussed in Section 5.1.

Reitz and Diwakar (1986) studied the role of drop collision and coalescence in sprays. They concluded that the spray drop size is the outcome of a competition between drop breakup and drop coalescence phenomena in non-vaporizing sprays. Drop breakup was found to dominate in hollow-cone sprays because coalescence is minimized by the expanding spray geometry. For solid-cone sprays, Reitz and Diwakar (1987) showed that drop coalescence becomes increasingly important at high gas densities.

This is shown in Figs. 4.16 and 4.17. The symbols in Fig. 4.16 show spray tip penetration versus time computations obtained using the KIVA code by

Reitz and Diwakar (1987) for the conditions of experiments of Hiroyasu and Kadota (1974) (shown by the lines). Tetradecane sprays were injected into room temperature nitrogen environments at gas pressures of 1.1, 3.0 and 5.0 MPa from a 0.3mm diameter nozzle. Details of the structure of these sprays were presented in Fig. 3.12. As can be seen, the agreement between the measurements and the computations is very good. The computed spray penetration is slightly higher than that measured, but this could be due to the lack of a precise definition for the location of the spray tip in both the experiments and the computations.

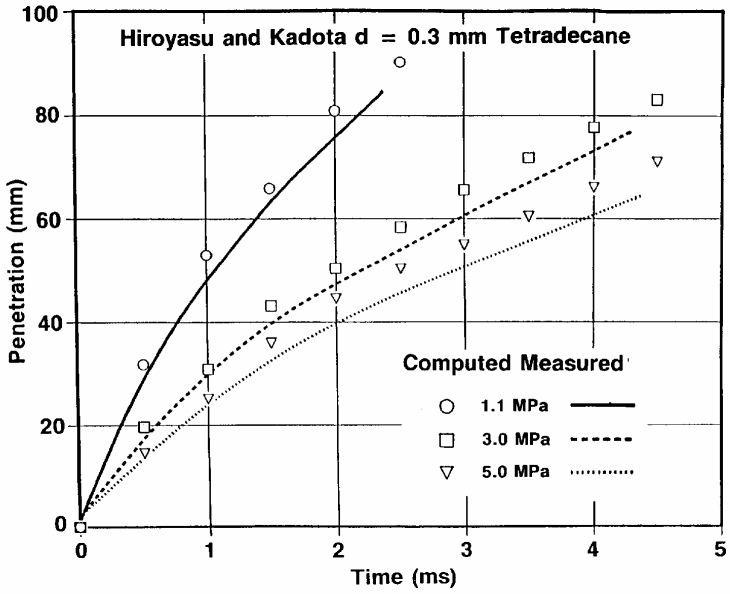

Fig. 4.16 Spray tip penetration computations of Reitz and Diwakar (1987) compared to measured data of Hiroyasu and Kadota (1974).

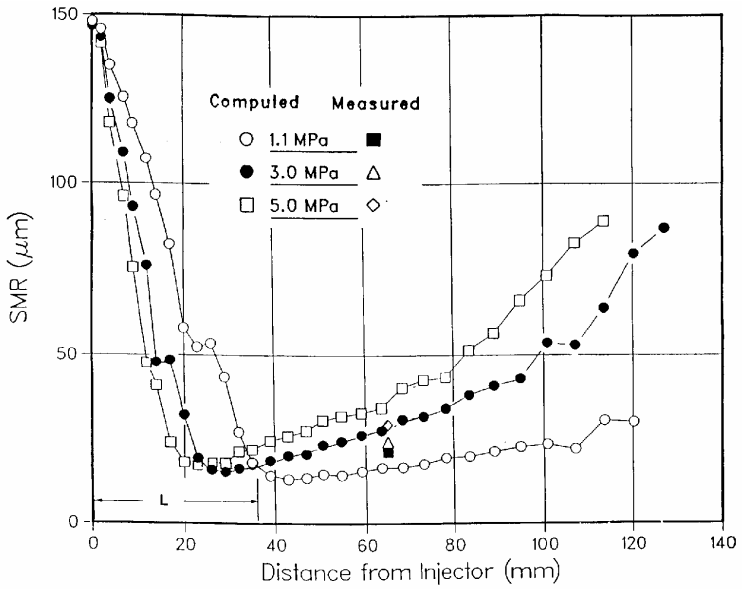

Fig. 4.17 Spray drop size computations of Reitz and Diwakar (1987) compared to measured data of Hiroyasu and Kadota (1974).

Figure 4.17 shows the corresponding SMR (Sauter Mean Radius) drop size predictions as a function of distance from the nozzle for steady sprays (the drop size is averaged over each spray cross-section). At the nozzle exit the drop size is equal to the nozzle radius, in accordance with the "blob" injection model (see Section 3.3). Due to breakup, the drop size decreases rapidly within a short distance of the nozzle, and the breakup length is seen to increase with reduced gas density, consistent with Eq. (3.6). The gradual increase in drop size beyond the core region is due to drop coalescences which become more important at high gas densities. This is because the increased drop drag at high gas densities (see Eqs. (4.21) causes the drops to decelerate faster, and the drop Weber number based on the drop relative velocities is thus reduced. This causes b_{crit} to increase, favoring coalescence (see Eq. 4.31). The increased efficiency of coalescence occurs in spite of the fact that the spray expands - the spray angle increases with increased gas density (see Eq. (3.7). Drop breakup also increases with increased gas density (see Eqs. 4.1 and 4.2) and the collision probability increases as the drop number density increases.

Drop size measurements made at 65 mm downstream of the nozzle exit by Hiroyasu and Kadota (1974) are also shown in Fig. 4.17. The predicted trend of increased drop size with increased gas density is evident in the measurements, but the predicted variation is larger than that measured. This disagreement could be related to the fact that the experimental sprays were pulsed, while the computed sprays assumed a constant pressure injection. Kuo and Bracco (1982) have shown that pulsed injections give the same spray tip penetration but smaller drops than steady injections. The difference in drop size is due to the inhibition of collisions and coalescences during the gaps between the pulses, and the differences become more marked at high gas densities, consistent with the results in Fig. 4.17.

An interesting consequence of the competition between drop breakup and drop coalescence is seen in Fig. 4.18, which shows three different predictions of drop size as a function of distance from the nozzle exit, made with and without including the effect of drop breakup in the computations, for the high pressure spray case of Fig. 4.17. In this case, the computations assumed initial drop radii of 2.0 and 35 μm at the nozzle exit (i.e., instead of using the "blob" injection model). As can be seen, when drop breakup is considered, the drop size downstream of the core region becomes independent of the size that is assumed for the drops at the nozzle exit. This shows that the spray drop size is determined by a local balance between drop breakups and coalescences. When drop breakup is not considered, the drop size increases due to coalescence (for the larger injected drop size case the increase in drop size was much less - not shown).

Notice that the results in Fig. 4.18 indicate that spray predictions are sensitive to the atomization process in the core region near the nozzle, and the core length can be comparable to the dimensions of the combustion chamber in internal combustion engine applications. Thus, engine results are sensitive to the models used to describe the atomization process at the nozzle (see Section 6.2).

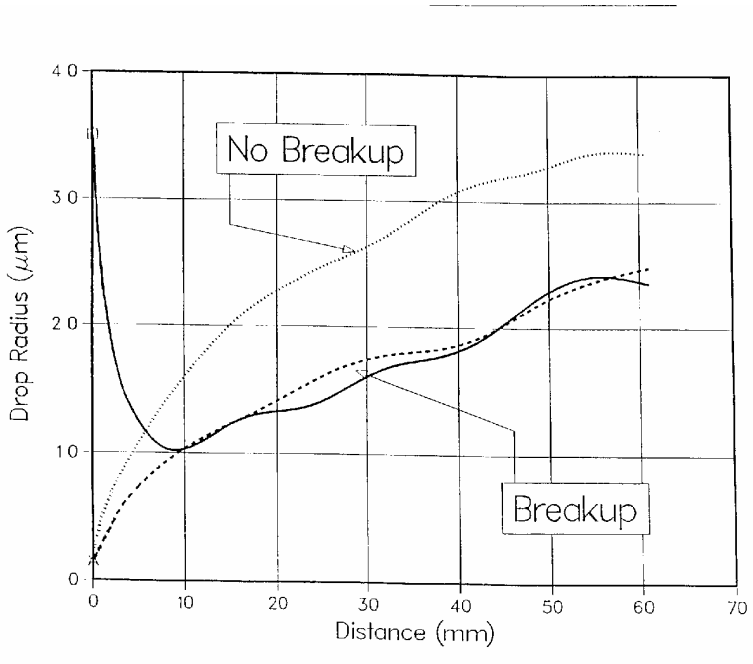

Fig. 4.18 Predicted drop size variation with distance from the nozzle, with and without considering drop breakup. The results show that the downstream drop size reflects a balance between drop breakup and coalescence in high pressure sprays.

Recent studies have indicated that improvements to the collision and coalescence models may be needed. For example, MacInnes and Bracco (1991) have shown that, in the absence of drop breakup and vaporization, the stochastic method of O'Rourke (1981) can underestimate drop collision and coalescence rates by up to a factor of two when compared with deterministic models. The error is partly due to the fact that the stochastic method assumes a uniform distribution of drops within a cell. In reality there can be significant changes in drop number density over distances of the order of the drop mean free path, and impractically fine grids would be needed to be able to resolve these gradients. However, MacInnes and Bracco (1991) point out that this error would be expected to decrease when the effects of drop breakup and vaporization are considered, because both of these effects tend to narrow the drop size and velocity distribution functions, which, in turn, reduces both collision and coalescence frequencies.

4.5 Drop Vaporization

In the KIVA codes (Amsden et al., 1985, 1989, 1993), the rate of drop radius change, R, in Eqs. (2.11) and (2.23) due to vaporization is found using the Frossling correlation (lefebvre, 1989)

$$\mathbf{R} = dr / dt = -\rho DBSh / (2\rho_1 r) \tag{4.32}$$

where *D* is the (laminar) mass diffusivity of fuel vapor in air whose density is ρ. B is the mass transfer number, $B = (Y_1^* - Y_1) / (1 - Y_1^*)$, where Y_1^* is the fuel mass fraction at the drop surface, Y_1 is the fuel mass fraction in the computational cell (ρ_1/ρ), and the subscript 1 refers to the fuel vapor. *Sh* is the Sherwood number

$$Sh = (2.0 + 0.6\,\mathrm{Re}_d^{1/2}\, Sc^{1/3})\frac{\ln(1+B)}{B} \tag{4.33}$$

and Sc is the Schmidt number of the air, ν/D. The fuel mass fraction at the drop surface is obtained by assuming the partial pressure of fuel vapor is equal to the equilibrium vapor pressure $p_v(T_d)$ at the drop temperature, T_d, i.e.

$$Y_1^* = W_1 / \{W_1 + W_0(\frac{p}{p_v(T_d)} - 1)\} \tag{4.34}$$

where, W_1 and W_0 are the fuel and air molecular weights, respectively, and p is the air pressure.

The change in drop temperature needed in Eqs. (2.22) and (2.25) is calculated from an energy balance involving the latent heat of vaporization and the heat conduction from the gas, i.e.,

$$\rho_d \frac{4}{3}\pi r^3 c_l \dot{T}_d - \rho_d 4\pi r^2 RL(T_d) = 4\pi r^2 Q_d \tag{4.35}$$

where c_l is the liquid specific heat, $L(T_d)$ is the latent heat of vaporization, and, Q_d, the rate of heat conduction to the drop, is given by the Ranz-Marshall correlation

$$Q_d = \alpha(T_2 - T_1)Nu / (2\rho r) \tag{4.36}$$

where α is the (laminar) thermal diffusivity, T_2 and T_1 are the gas and drop temperatures, respectively, and *Nu* is the Nusselt number

$$Nu = (2.0 + 0.6\,\mathrm{Re}_d^{1/2}\,\mathrm{Pr}^{1/3})\frac{\ln(1+B)}{B} \qquad (4.37)$$

where Pr is the air Prandtl number ν/α. Tabulated data is used to describe the thermodynamic properties of the liquid and the gas as functions of pressure, temperature and composition. Other details about the implementation of the drop vaporization model are described by Amsden et al. (1989).

Improvements to the above drop vaporization model have been proposed. For example, Renksizbulut and Yuen (1983) have shown that vaporization reduces heat transfer rates and drag coefficients. They suggest using

$$C_d = \frac{24}{\mathrm{Re}_d}(1 + 0.2\,\mathrm{Re}_d^{0.63})/(1+B)^{0.2} \qquad (4.38)$$

instead of Eq. (4.22a). The use of Eq. (4.38) in KIVA was explored by Gonzalez et al. (1992) who found that the effect of vaporization on drop drag was small for diesel-type sprays.

Gonzalez et al. (1992) also explored the vaporization model of Priem et al. (1957) that accounts for the fact that the liquid density varies with liquid temperature (which is important during the heat-up period of the drop), and is not considered in the standard KIVA model. The Priem model also includes a correction to the heat transfer to account for the superheating of the diffusing vapor around the drop, i.e.,

$$Q_d = \alpha(T_2 - T_1)Nu/(2\rho r)\frac{Z}{\exp(Z)-1} \qquad (4.39)$$

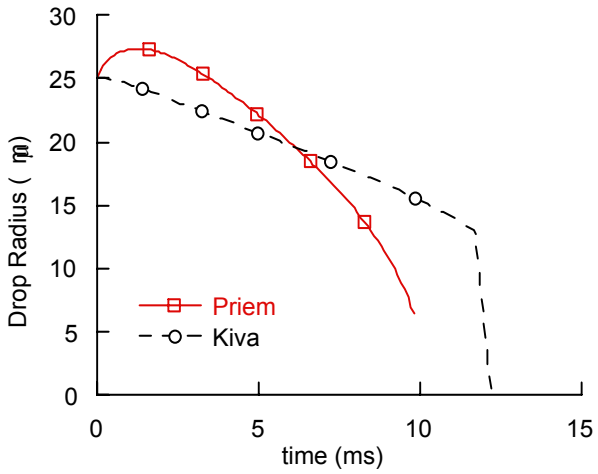

Fig. 4.19 Calculated drop radius versus time using standard KIVA and Priem vaporization models with initial drop velocity 100 m/s (Gonzalez et al., 1992).

where $Z = -c_l \dot{m}_d / (2\pi r \alpha \rho_d Nu)$, and $\dot{m}_d$ is the rate of change of drop mass with time. A single 50 μm diameter room-temperature hexadecane drop was injected into a quiescent nitrogen environment at 800 K and 4.0 MPa. Figure 4.19 shows the variation of the drop radius with time. The standard KIVA model predicts somewhat longer drop lifetimes than the more comprehensive Priem model. The swelling of the drop at early times in the Priem model is due to the effect of the variable density during the heat-up period. The rapid change in drop size toward the end of the drop's lifetime in both models corresponds to the time when the liquid's critical temperature is reached.

Drop sizes in vaporizing sprays are also influenced by condensation. This is shown in Fig. 4.20 which gives the predicted rate of change of drop radius, dr/dt, as a function of drop diameter for all of the drops in a vaporizing spray computation (i.e., regardless of their location in the spray). dr/dt is seen to be negative (i.e., vaporization) only for the very small drops. For drops larger than about 4 μm in diameter, condensation is predicted since dr/dt >0 (these computations did not include variable liquid density which could also cause the drop size to increase upon heating).

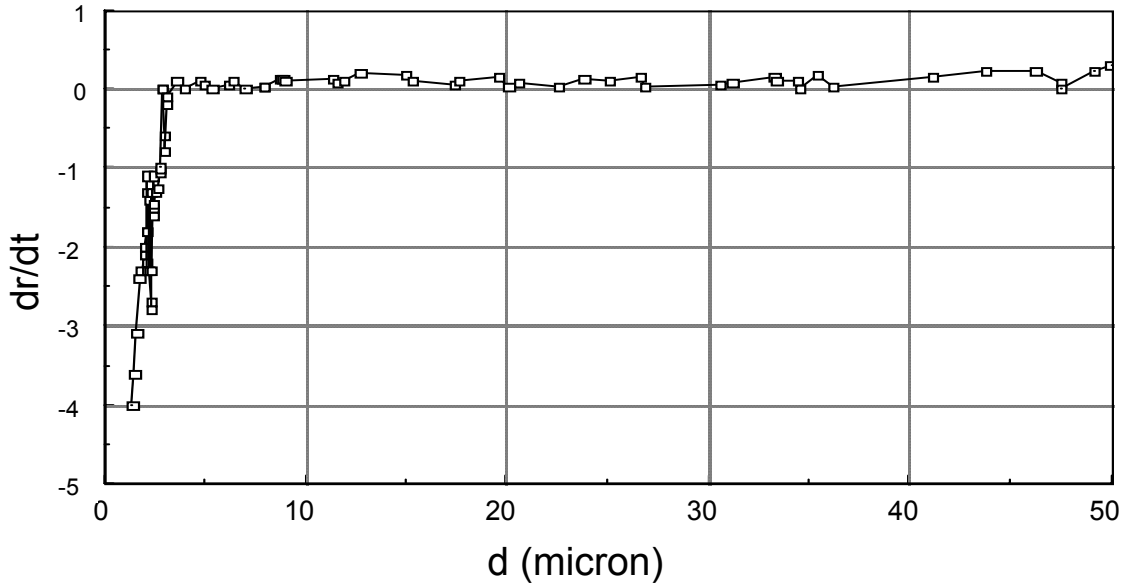

Fig. 4.20 Rate of change of drop radius as a function of drop diameter for a vaporizing diesel spray (n-tridecane injections into nitrogen at 875K and 3 MPa (Gonzalez et al., 1992).

Condensation occurs due to the fact that the large spray drops are relatively cool and they are surrounded by saturated vapor formed from the fast vaporization of the small, high temperature, drops.

The assumption of uniform drop temperature is justified if the thermal capacity of the gas is much smaller than that of the drops. For spray drops this ratio is about 0.3, and the drop internal temperature may not be uniform (Ramos, 1989). In this case it is also necessary to solve for the flow field within the drop. Detailed reviews of advanced droplet vaporization models are given by Sirignano (1983, 1993). These models also account for internal circulation within the drops and multicomponent fuels.

Most applications of advanced vaporization models have been to single drops or to simple arrays of drops. However, Raju and Sirignano (1988) studied 2-D multicomponent spray vaporization in the near wake region of a ducted bluff-body combustor using a simplified spray model that ignores drop breakup and

coalescence effects. Ayoub and Reitz (1994) implemented the multicomponent fuel vaporization model of Jin and Borman (1985) into the KIVA code which includes drop breakup and coalescence. The vaporization model uses phase equilibrium relations at the drop surface to evaluate the composition of each species in both the liquid and vapor phases. These boundary conditions are then used for the mass and heat diffusion equations which are solved on a (coarse) finite difference grid of 10 points inside each drop - greatly increasing the computer storage requirements for KIVA. The effect of drop internal circulation is modeled using an "effective" diffusivity model (Jin and Borman, 1985). The composition and temperature of drops formed during the atomization process is assumed to be that of the surface layer of the "parent" drop. In the case of collision and coalescence of two droplets, if collision occurs without coalescence, it is assumed that there is no mixing of the contents of the drops. However, when coalescence occurs, the contents are assumed to be well mixed.

Ayoub and Reitz (1994) applied the model to a 50-50% molar mixture of dodecane and hexadecane injected with an injection pressure of 90 MPa into nitrogen at 6 MPa and 800 K or 500 K (800 K simulates normal diesel engine compression temperatures; 500 K simulates conditions under cold-starting). Figure 4.21 shows the ratio of the vaporized mass of the volatile component ($C_{12}H_{26}$) to the total vaporized mass in the spray as a function of time after the start of injection. When all the fuel is vaporized the initial mass composition of the fuel mixture is reached (i.e., 0.43 or 0.50 by mole). As can be seen, there is significant deviation from "ideal" vaporization, indicating the importance of multicomponent fuel vaporization, particularly the under colder temperature conditions.

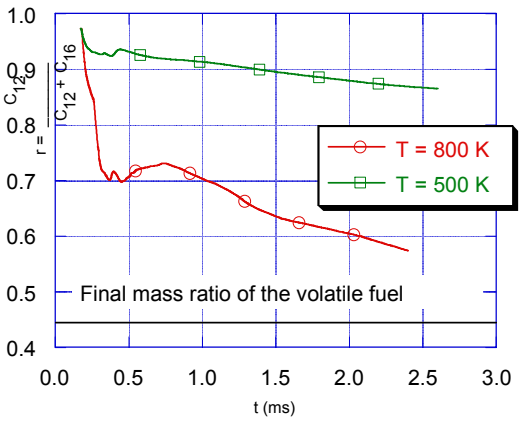

Fig. 4.21 Ratio of volatile vaporized mass to the total vaporized mass in a multicomponent diesel spray (Ayoub and Reitz, 1994).